

Can Explicit Subgrid Models Enhance Implicit LES Simulations? A GPU-Oriented High-Order-Solver Perspective

Gonzalo Rubio^{a,b,*}, Gerasimos Ntoukas^c, Miguel Chávez-Módena^{a,b}, Oscar Mariño^{a,b},
Bernat Font^d, Oriol Lehmkuhl^e, Eusebio Valero^{a,b}, Esteban Ferrer^{a,b}

^a*ETSIAE-UPM - School of Aeronautics, Universidad Politécnica de Madrid, Madrid, Spain*

^b*Center for Computational Simulation, Universidad Politécnica de Madrid, Madrid, Spain*

^c*Simerics Inc, Bellevue, WA, United States*

^d*Faculty of Mechanical Engineering, Technische Universiteit Delft, The Netherlands*

^e*Barcelona Supercomputing Center, Barcelona, Spain*

Abstract

High-order Discontinuous Galerkin (DG) methods offer excellent accuracy for turbulent flow simulations, especially when implemented on GPU-oriented architectures that favor very high polynomial orders. On modern GPUs, high-order polynomial evaluations cost roughly the same as low-order ones, provided the DG degrees of freedom fit within device memory. However, even with high-order discretizations, simulations at high Reynolds numbers still require some level of under-resolution, leaving them sensitive to numerical dissipation and aliasing effects. Here, we investigate the interplay between intrinsic DG dissipation mechanisms (implicit dissipation)—in particular split forms and Riemann solvers—and explicit subgrid-scale models in Large Eddy Simulations (LES). Using the three-dimensional Taylor–Green vortex at $Re = 1600$ and an inviscid case ($Re \rightarrow \infty$), we evaluate kinetic energy dissipation, spectral accuracy, and numerical stability.

Our results show that when stability for under-resolved turbulence is ensured through split-forms (energy- or entropy-stable) schemes, subgrid scale (SGS) LES models are not strictly necessary. At moderate Reynolds numbers, when the spatial resolution is sufficient to capture the relevant turbulence scales (i.e., in well-resolved LES), adding SGS models does not improve accuracy because the wavenumber range where they act overlaps with the inherent numerical dissipation of the DG scheme. In contrast, when the resolution is insufficient, as is typical at high Reynolds numbers, explicit subgrid-scale models complement the numerical dissipation and enhance accuracy by removing the excess energy that numerical fluxes alone

*Corresponding author.

Email address: g.rubio@upm.es (Gonzalo Rubio)

cannot dissipate.

These findings provide practical guidance for choosing numerical strategies in high-order turbulence simulations.

Keywords: Spectral element methods, Discontinuous Galerkin, Split form, Large Eddy Simulation, Riemann solvers, Taylor–Green vortex, GPU

1. Introduction

High-order Discontinuous Galerkin (DG) methods have emerged as a powerful tool for the numerical simulation of complex fluid flows due to their ability to achieve arbitrary polynomial accuracy within each mesh element [1, 2, 3, 4]. Unlike low-order schemes, high-order DG methods concentrate numerical errors at high wavenumbers, resulting in low dispersive and dissipative errors for well-resolved flows. This property ensures highly accurate representations of energy-containing scales and is particularly advantageous in Direct Numerical Simulation (DNS) and Large Eddy Simulation (LES) of turbulent flows.

However, the high fidelity of DG methods also introduces challenges in under-resolved computations, such as implicit Large Eddy Simulations (iLES). In these situations, the grid or polynomial resolution is insufficient to capture the smallest turbulent scales, leading to numerical under-resolution and aliasing [5]. Without adequate dissipation, energy accumulates at unresolved scales, potentially destabilizing the simulation; hence, under-resolved turbulent flows computed with high-order DG solvers require carefully designed stabilizing mechanisms that act locally near the cut-off scales.

A variety of stabilization strategies have been proposed to mitigate aliasing and improve robustness in high-order DG schemes. These include split forms or skew-symmetric variants of the convective terms [6, 7], interior penalty fluxes [8], over-integration [9, 10, 11], and explicit or implicit filtering [12]. In particular, energy- and entropy-stable schemes exploit Gauss–Lobatto quadrature and the Summation–By–Parts Simultaneous-Approximation-Term (SBP–SAT) property [13, 14, 15, 16, 17] to mimic continuous conservation of energy or entropy at the discrete level. These schemes provide intrinsic robustness, allowing under-resolved simulations to remain stable without relying on excessive numerical dissipation. Recent developments have extended these principles to the Spalart–Allmaras RANS equations [18] and to multiphase flows with p-adaptation [19, 20], demonstrating their versatility across flow regimes.

The work of Winters et al. [21] highlighted the fundamental limitations of iLES approaches when using high-order DGSEM with split forms in under-resolved turbulence. They observed that, at very high orders (eighth order and above), stable solutions exhibited unphys-

ical features, which were attributed to an energy-conserving bias resulting from the sharper dissipative behavior in wavenumber space. This limitation of iLES approaches has recently renewed interest in the use of explicit subgrid-scale (SGS) modeling within high-order discretizations. Early LES developments showed that appropriate SGS closures, such as the classical Smagorinsky model [22, 23], are crucial to stabilizing strongly under-resolved turbulent simulations. Subsequent formulations, including the WALE [24] and Vreman [25] models, aimed to reduce excessive damping and recover the correct near-wall scaling of the eddy viscosity. The necessity of explicit SGS modeling is intrinsically related to the dissipative characteristics of the numerical scheme. High-order discontinuous Galerkin (DG) methods are inherently low-dissipative, so the inclusion of a SGS model must carefully balance stability and spectral fidelity. Excess model dissipation can attenuate large-scale dynamics, while its absence may lead to an accumulation of energy near the grid cut-off [26, 27]. Duan and Wang [28] recently argued that, in wall-modeled LES (WMLES), high-order methods benefit from additional SGS dissipation. They recommend using the Vreman model with a modified filter length that effectively increases the model constant compared to finite-volume implementations. In contrast, for wall-resolved LES (WRLES), a purely implicit approach remains preferable. This conclusion aligns with previous applications of the Vreman model in high-order WMLES studies, which have demonstrated improved stability and accuracy in under-resolved regimes [29, 30]. Kumar et al. [31] conducted a systematic study of WRLES using high-order schemes and found that the reduced model constants yield improved agreement with the reference data. Comparative assessments of explicit and implicit SGS strategies in DG formulations have also been reported in [32, 33], underscoring the sensitivity of high-order LES to both modeling and discretization choices. More recently, data-driven approaches have explored adaptive and discretization-consistent closures. Reinforcement learning has been used to dynamically adjust the SGS constant and enforce consistency between modeled and numerical dissipation [34, 35]. These advances reflect a broader trend toward hybrid, adaptive SGS formulations capable of reconciling physical and numerical dissipation across scales.

The distinction between low- and high-order discretizations has become increasingly significant in recent years with the widespread adoption of GPU-based computing. Modern GPUs favor computationally intensive workloads over memory-bound operations, which aligns naturally with the characteristics of high-order methods. Since increasing the degree of polynomial enhances the arithmetic intensity while reducing memory traffic, high-order DG formulations can achieve superior performance and energy efficiency on GPU architectures. Recent studies have shown that very high polynomial orders (typically around $P = 6-8$) deliver the best balance between accuracy and computational throughput [36, 37, 38].

In this work, we revisit this question in a fundamental configuration: the three-dimensional Taylor–Green vortex at both finite ($Re = 1600$) and infinite Reynolds numbers. We systematically examine the interplay between different stabilization mechanisms—split forms, Riemann solvers, and explicit SGS models—to quantify their impact on spectral accuracy, energy dissipation, and robustness. Particular attention is paid to very high polynomial orders ($P = 7$), which are increasingly relevant due to the computational efficiency achievable on modern GPU architectures. A key question we seek to address is whether the unphysical features reported by Winters et al. [21] for split-form DG schemes at very high orders can be mitigated through the use of explicit SGS modeling. Our findings confirm that explicit SGS models can indeed mitigate the unphysical features observed in split-form DG schemes at very high polynomial orders, particularly when the inherent numerical dissipation is insufficient to prevent such unphysical behavior (e.g., energy accumulation). However, the effectiveness of this mitigation—and the appropriate modeling strategy—depends critically on resolution (i.e., combination of grid resolution and Reynolds number). Specifically, the optimal approach for a well-resolved LES differs fundamentally from that required in under-resolved conditions, both in terms of stabilization mechanisms and the role of SGS dissipation.

The remainder of the paper is organized as follows. Section 2 details the numerical methodology, and Section 3 introduces the test cases. The numerical experiments and results are presented in Section 4, followed by a discussion in Section 5, and the conclusions are summarized in Section 6.

2. Numerical Methodology

2.1. DGSEM Formulation

The compressible Navier–Stokes equations are solved in conservative form (see Appendix A) using the Discontinuous Galerkin Spectral Element Method (DGSEM), a nodal high-order variant of the Discontinuous Galerkin (DG) method [39, 40]. The DGSEM combines high-order accuracy with geometric flexibility and parallel scalability, making it well suited for large-scale turbulence simulations.

Two standard choices exist for the nodal distribution in DGSEM: Legendre–Gauss nodes and Legendre–Gauss–Lobatto nodes (hereafter, Gauss and Gauss–Lobatto nodes, respectively). Gauss nodes offer improved accuracy, while Gauss–Lobatto nodes enable slightly larger stable time steps for explicit time integrators [41]. In this work, we employ Gauss nodes only for the preliminary assessment in Sec. 4.1.1, and adopt Gauss–Lobatto nodes for all subsequent simulations.

To ensure robustness in under-resolved conditions, the convective fluxes are discretized using energy- or entropy-preserving split forms, while controlled numerical dissipation is introduced via Riemann solvers (e.g., Roe-type fluxes). These intrinsic stabilization mechanisms can be complemented by explicit subgrid-scale (SGS) models for LES. The interplay between these three sources of dissipation—split forms, Riemann solvers, and SGS models—is systematically assessed in this work.

Viscous terms are discretized using the Bassi–Rebay 1 (BR1) scheme, which is equivalent to the interior penalty formulation when Gauss–Lobatto points and hexahedral elements are used [42]. The BR1 approach is neutrally stable [43], introducing only the minimal dissipation required for stability, unlike alternative formulations that include additional damping [44]. A detailed description of the DGSEM formulation is provided in [Appendix B](#).

2.2. Energy- and Entropy-Stable Split Forms

High-order DG schemes can be formulated to preserve discrete analogues of continuous energy or entropy conservation by employing Gauss–Lobatto quadrature points for numerical integration. This property is enforced through the Summation–By–Parts Simultaneous Approximation Term (SBP–SAT) framework [13, 14, 45, 46, 4, 47], which enhances robustness in under-resolved turbulent flows and reduces aliasing errors [48]. Recent work has shown that the diagonal-norm SBP operator on Gauss nodes can also be expressed in flux-differencing form [49], thereby enabling the extension of stabilization techniques originally developed for Gauss–Lobatto nodes to Gauss nodes. Nevertheless, in this study we restrict ourselves to the traditional split-form formulations based on Gauss–Lobatto nodes. For an in-depth discussion of the respective advantages and drawbacks of split forms on Gauss and Gauss–Lobatto nodes, the reader is referred to the recent analysis in [15].

Extensive literature exists on energy- and entropy-stable DG schemes [13, 50, 47, 51, 52, 53, 21, 54], with reviews available in [47, 55, 56]. In these schemes, convective terms are rewritten in split form using two-point fluxes, which improves stability while preserving energy or entropy at the discrete level, at a modest additional computational cost. In this study, we compare several representative formulations, including the standard [47], Morinishi [57, 47], Ducros [58, 47], Kennedy–Gruber [59], Pirozzoli [60], entropy-conserving [61], and Chandrasekhar forms [62].

2.3. Riemann Solvers

Riemann solvers are the standard approach to introduce numerical dissipation in DG schemes [63, 64], as they arise naturally from the discretization of the non-linear convective terms.

These solvers provide controlled dissipation, which can be further supplemented by turbulence models for high-Reynolds-number flows. Comparative studies of Riemann fluxes in homogeneous turbulence can be found in [65, 66].

The solvers evaluated in this study include both central and upwind-biased fluxes, covering a wide range of dissipative behaviors. The central flux represents the non-dissipative limit, while classical upwind formulations such as Roe’s approximate Riemann solver [67] introduce controlled dissipation through characteristic decomposition. The low-dissipation Roe variant of Osswald et al. [68] and the matrix dissipation flux of Ismail and Roe [61] reduce numerical damping while retaining robustness in under-resolved regions. In contrast, the Lax–Friedrichs scheme [69] provides strong dissipation and is often used for stabilization in highly convective regimes.

2.4. Subgrid-Scale Modeling

For the explicit LES cases, we employ the Vreman SGS model [25], selected for its robustness and proven suitability within high-order DG frameworks [28]. The model defines the eddy viscosity in a way that satisfies the physical requirement of vanishing turbulent viscosity near solid walls.

The SGS viscosity is expressed as

$$\begin{aligned}\mu_t &= C_v \rho \sqrt{\frac{B_\beta}{\alpha_{ij}\alpha_{ij}}}, \quad \alpha_{ij} = \frac{\partial u_j}{\partial x_i}, \\ \beta_{ij} &= \Delta^2 \alpha_{mi} \alpha_{mj}, \quad \Delta = \frac{V^{1/3}}{P+1}, \\ B_\beta &= \beta_{11}\beta_{22} - \beta_{12}^2 + \beta_{11}\beta_{33} - \beta_{13}^2 + \beta_{22}\beta_{33} - \beta_{23}^2\end{aligned}\tag{1}$$

where C_v is the model constant, V the element volume, and P the polynomial order. The influence of C_v on the solution is analyzed in this work, and the coupling of the SGS model to the compressible Navier–Stokes equations is detailed in [Appendix A](#).

2.5. Time Integration

Temporal integration is performed using the low-storage, third-order explicit Runge–Kutta scheme (RK3) [70]. A fixed timestep is employed, determined based on Courant–Friedrichs–Lewy (CFL) considerations to ensure stability. This scheme provides a balance between computational efficiency and temporal accuracy and is used consistently in all simulations presented.

2.6. Solver Implementation

All simulations in this work are performed using the high-order spectral element solver **HORSES3D** [40, 38], developed at ETSIAE–UPM. The code implements the DGSEM formulation on curvilinear hexahedral meshes of arbitrary order and supports all the numerical ingredients described above, including energy- and entropy-stable split forms, multiple Riemann solvers, the BR1 viscous discretization, explicit SGS models, and explicit Runge–Kutta time integration. **HORSES3D** is fully parallelized for large-scale computations on CPU and GPU clusters. Almost ideal scaling has been obtained in 9000 CPU processors and 256 GPUs.

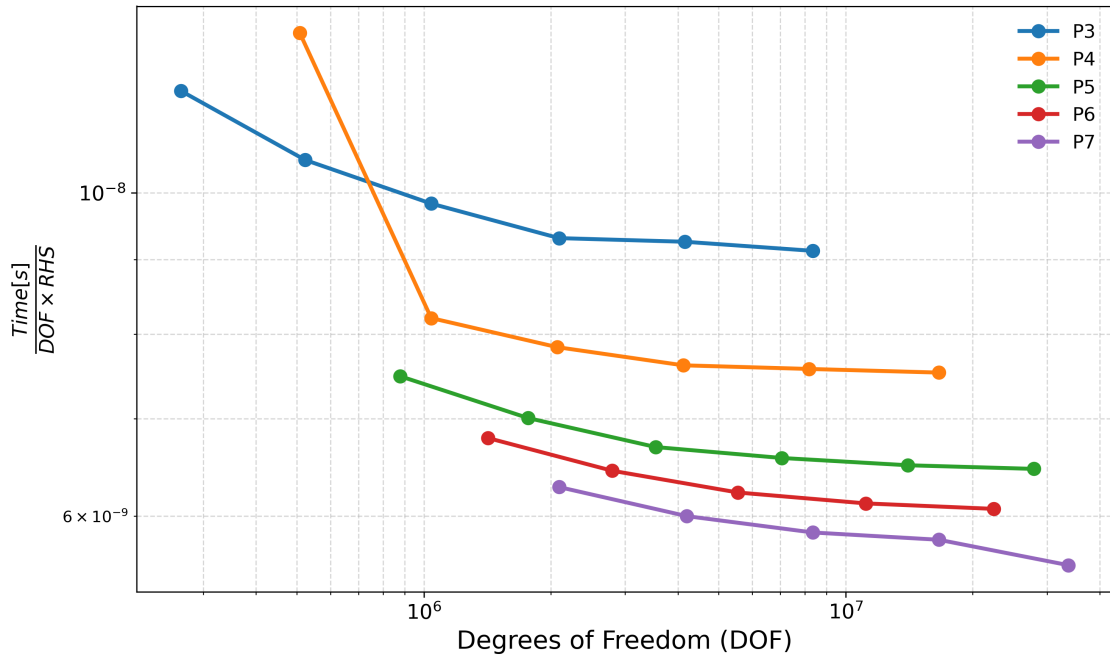


Figure 1: GPU efficiency of **HORSES3D** on a single GPU. Efficiency increases with P , roughly doubling from $P = 3$ to $P = 7$, due to higher arithmetic intensity and reduced memory traffic.

Although the present work is not focused on GPU performance, we include a brief assessment for completeness. The GPU performance of **HORSES3D** is evaluated using the metric

$$\frac{\text{Time}}{\text{DOF} \times \text{RHS}}, \quad (2)$$

which measures the cost of evaluating the right-hand side (RHS) per degree of freedom (DOF). Tests on a single NVIDIA H100 HBM2 GPU with varying mesh sizes and polynomial orders ($P = 3\text{--}7$) show that efficiency increases with the polynomial order, see Fig. 1.

Specifically, moving from $P = 3$ to $P = 7$ roughly doubles efficiency. This improvement arises because higher-order DGSEM packs more data per kernel, increasing arithmetic intensity and reducing memory traffic.

3. Test Case Definition

3.1. Taylor–Green Vortex

The canonical three-dimensional Taylor–Green vortex (TGV) in Reynolds numbers $Re = 1600$ and $Re \rightarrow \infty$ is used to evaluate the performance of numerical schemes and their ability to capture the laminar–turbulent transition. In particular, the inviscid case is representative of viscous TGV solutions at very high Reynolds numbers [21]. The domain is a cube of size $L = 2\pi$, discretized with a uniform Cartesian grid of 16^3 hexahedral elements, with periodic boundary conditions on all sides. A polynomial order of $P = 7$ is employed within each element. Time integration is performed with a fixed time step $\Delta t = 2 \times 10^{-4}$.

Initial condition. The initial velocity and thermodynamic fields are set according to the standard divergence-free TGV formulation:

$$\begin{aligned} \rho &= \rho_0, \\ u &= u_0 \sin\left(\frac{x}{L_0}\right) \cos\left(\frac{y}{L_0}\right) \cos\left(\frac{z}{L_0}\right), \\ v &= -u_0 \cos\left(\frac{x}{L_0}\right) \sin\left(\frac{y}{L_0}\right) \cos\left(\frac{z}{L_0}\right), \\ w &= 0, \\ p &= \frac{\rho_0 u_0^2}{\gamma M_0^2} + \frac{\rho_0 u_0^2}{16} \left[\left(\cos(2x/L_0) + \cos(2y/L_0) \right) \left(\cos(2z/L_0) + 2 \right) \right], \end{aligned} \tag{3}$$

with $\gamma = 1.4$, $M_0 = 0.1$, $\rho_0 = 1$, $u_0 = 1$, and $L_0 = 1$. Time is non-dimensionalized as t/t_c , where the characteristic time $t_c = L_0/u_0$.

The initial flow is smooth, as the simulation progresses beyond $t/t_c \gtrsim 6$, the flow transitions from the laminar initial state to a turbulent anisotropic regime, and beyond $t/t_c \gtrsim 13$, fully developed turbulence with isotropic structures emerges.

Diagnostics. To evaluate the performance of different numerical schemes, we monitor the *kinetic energy* and its *dissipation rate*, which provide insight into stability, energy transfer, and spectral fidelity. The kinetic energy is defined as

$$E = \frac{1}{\rho_0 V} \int_V \frac{1}{2} \rho \mathbf{u} \cdot \mathbf{u} dV, \quad \mathbf{u} = (u, v, w)^T, \quad V = \text{domain volume},$$

with dissipation rate

$$\text{dissipation rate} = -\frac{dE}{dt}.$$

Two complementary diagnostics are used to analyze each simulation:

- **Kinetic energy dissipation rate over time** — indicates global energy decay and the stability of the numerical scheme.
- **Kinetic energy spectrum at $t/t_c = 9$** — quantifies the distribution of energy across scales, providing a measure of spectral fidelity.

The Nyquist wavenumber for the kinetic energy spectrum is

$$k_{\text{Ny}} = \frac{\pi}{\Delta x}, \quad \Delta x = \frac{L}{(P+1)N_{\text{el}}}, \quad (4)$$

where L is the domain length, P the polynomial degree, and N_{el} the number of elements per spatial direction [71, 72].

References. The kinetic energy dissipation of the TGV at $\text{Re} = 1600$ is compared against the dispersion-relation-preserving (DRP) solution on a 512^3 mesh reported by Bull and Jameson [72]. The energy spectra are compared with the pseudospectral results obtained on a 512^3 grid by Carton de Wiart *et al.* [73]. For the inviscid TGV, the kinetic energy dissipation is compared with the reference data from Fehn *et al.* [71], computed with an effective resolution of 8192^3 . The corresponding energy spectra are also compared with the same reference, using an effective resolution of 2048^3 .

4. Numerical experiments

This section systematically evaluates the performance of high-order DG discretizations for the three-dimensional Taylor–Green vortex. We analyze the effects of split-form formulations, Riemann solvers, and explicit SGS on stability, energy dissipation, and spectral accuracy. Each study isolates a key numerical ingredient, from intrinsic stabilization by split forms and explicit Vreman SGS dissipation to the influence of different Riemann solvers and their hybrid combinations. The most robust configurations are further tested in the inviscid limit to assess the role of numerical dissipation when physical viscosity is absent.

4.1. *Well-Resolved LES (The Viscous Taylor–Green Vortex): Implicit and Explicit Dissipation Mechanisms*

We consider the Taylor–Green Vortex at Reynolds 1600, representing a well-resolved LES. The goal is to assess whether iLES can be improved by adding an explicit SGS model. Stability is first ensured using split forms, after which we compare dissipation mechanisms for accuracy, contrasting implicit iLES (Riemann fluxes) with explicit SGS contributions. Finally, a hybrid approach combining Riemann solvers and SGS modeling is tested to evaluate potential improvements.

4.1.1. *Standard vs Split-Form Discretizations*

In this preliminary analysis, we evaluate the effect of split-form (e.g., Chandrasekar) formulations in comparison to standard discretizations. Note that the split-form schemes employ Gauss–Lobatto nodes, while in this subsection the standard discretization uses Gauss nodes. Simulations using the standard approach exhibit numerical instabilities and eventually diverge. In particular, the central configuration becomes unstable around $t/t_c \approx 4$, while the Roe variant remains stable for a longer period but fails near $t/t_c \approx 7$. These observations indicate that, in the absence of split-form stabilization, aliasing errors accumulate as nonlinear interactions intensify, ultimately leading to blow-up during the transitional regime. The Riemann solver alone does not provide sufficient dissipation to stabilize the simulation.

Fig. 2 presents the time evolution of the kinetic energy dissipation rate, highlighting the onset of instability for both standard discretizations. For comparison, the figure also includes the behavior of a representative split-form scheme. Around $t/t_c \approx 5$, the split form introduces additional dissipation, effectively stabilizing the simulation and preventing blow-up.

These findings highlight the critical role of split-form discretizations in ensuring robustness for under-resolved simulations. By introducing additional nonlinear stabilization, split forms effectively control aliasing errors throughout the laminar–turbulent transition.

4.1.2. *Performance of Central Split Forms*

This part investigates the performance of multiple central split-form discretizations without explicit SGS modeling. As in the remainder of the paper, all formulations—including the standard (non split-form) discretization—employ Gauss–Lobatto nodes. Interface fluxes are computed using minimally dissipative central fluxes combined with the BR1 scheme for viscous terms. This setup isolates the intrinsic stabilization provided by each split form.

Among the tested formulations, Ducros, Kennedy–Gruber, Pirozzoli, Entropy-conserving, and Chandrasekhar split forms remain stable throughout the simulation and exhibit nearly identical kinetic energy dissipation rates (Fig. 3a). In contrast, the Standard and Morinishi schemes become unstable early, at $t/t_c \approx 3.5$ and $t/t_c \approx 5$, respectively.

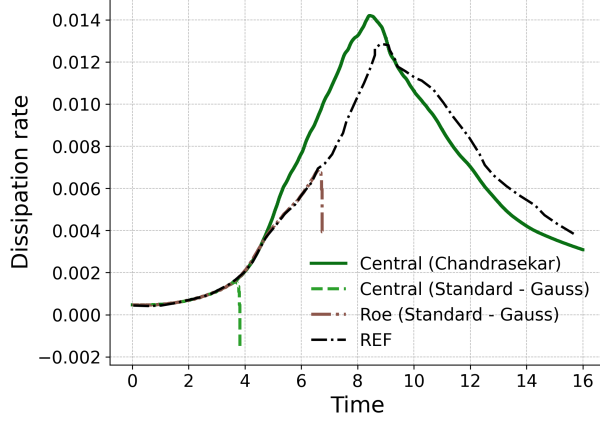
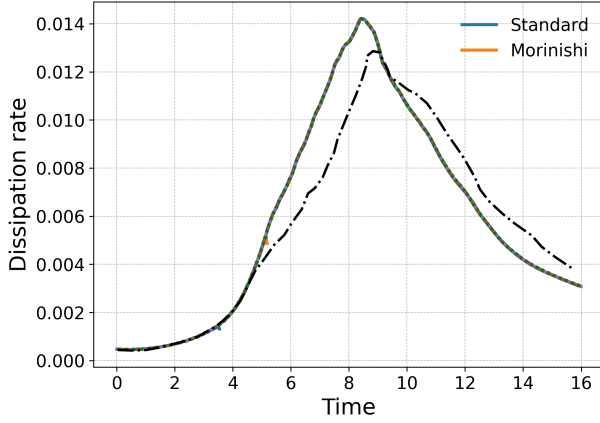
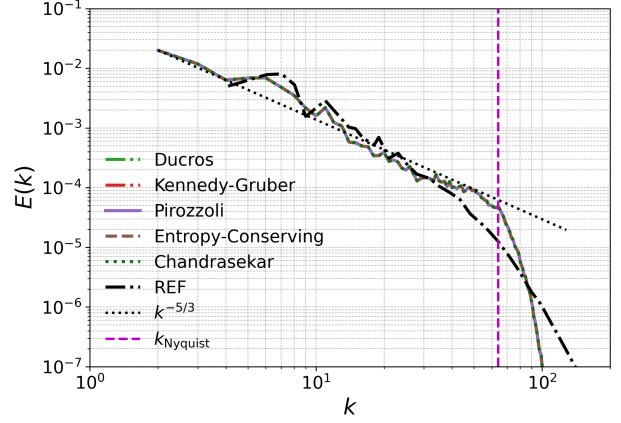


Figure 2: Kinetic energy dissipation rate for standard (non-split) formulations with Gauss nodes. Both central and Roe-based fluxes eventually diverge due to aliasing-driven instabilities, while the split-form scheme introduces stabilizing dissipation.



(a) Kinetic energy dissipation rate.



(b) Kinetic energy spectrum at $t/t_c = 9$.

Figure 3: Effect of central split forms on dissipation and spectral behavior. The standard and Morinishi schemes are shown only in Fig. 3a, as they became unstable before $t/t_c = 9$. Results for all schemes are shown in both figures, and the curves overlap, indicating only minimal differences between the methods. Overall, central split forms exhibit excess dissipation during transition and insufficient dissipation once turbulence is fully developed.

During the transitional phase ($t/t_c \in [4, 8]$), all stable split forms display a dissipation peak exceeding that in the reference data. This enhanced dissipation is attributable to aliasing-driven implicit numerical dissipation, which compensates for the under-resolution of small scales, as noted in [72].

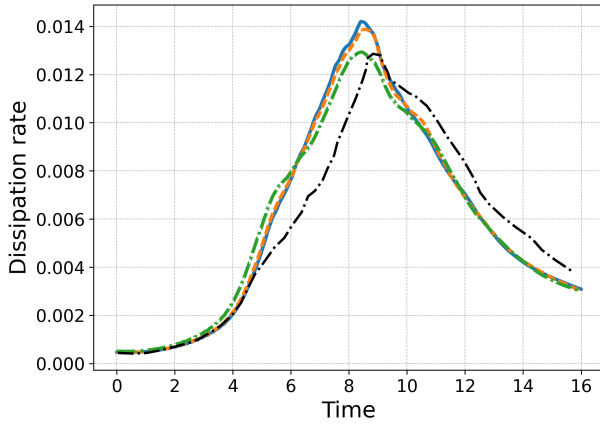
In the fully turbulent regime ($t/t_c > 8$), the kinetic energy decays smoothly and the resulting

spectra closely follow the reference slopes for moderate wavenumbers. At high wavenumbers ($k > 30$), some energy accumulation is observed due to insufficient dissipation in the smallest resolved scales (Fig. 3b).

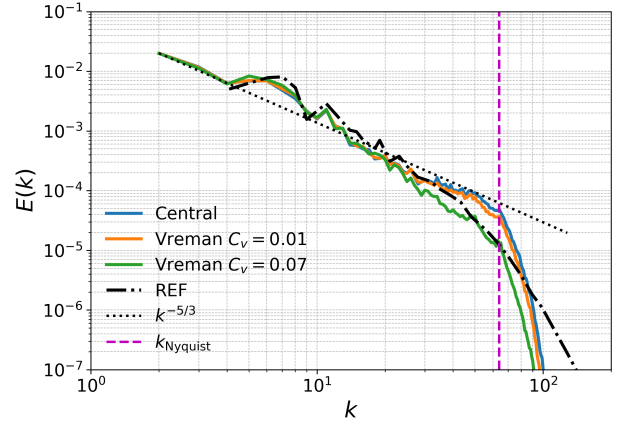
Overall, central split forms provide intrinsic stabilization sufficient for under-resolved simulations. However, when used without additional dissipation mechanisms, they tend to over-dissipate energy during the transitional phase and under-dissipate at high wavenumbers in the turbulent regime, affecting the spectral distribution of energy. Most split-form discretizations exhibited comparable behavior for this low-Mach-number case, with the exception of the standard and Morinishi formulations. For the remainder of the paper, the Chandrasekhar split form is adopted, as it has previously been shown to provide improved robustness in complex and highly compressible flows [74, 15].

4.1.3. Impact of the Vreman SGS Model

In this section, the Chandrasekhar split form is combined with an explicit Vreman SGS model of varying strength to evaluate its influence on the accuracy of the numerical scheme. The Vreman model introduces tunable dissipation at unresolved scales [25] (see Appendix A for details). Two model constants are considered: $C_v = 0.07$, the standard value in finite-volume methods [75], and $C_v = 0.01$, a smaller value suggested for high-order methods [31].



(a) Kinetic energy dissipation rate.



(b) Kinetic energy spectrum at $t/t_c = 9$.

Figure 4: Effect of the Vreman SGS model on the Chandrasekhar split form. The model does not improve the accuracy of the transitional dynamics, while in the fully turbulent regime larger constants recover the expected spectral decay at high wavenumbers. Increasing the constant shifts model-induced dissipation toward lower wavenumbers, overdamping intermediate scales, while smaller constants under-dissipate the highest wavenumbers.

During the early transitional phase ($t/t_c \in [4, 6]$), the larger constant ($C_v = 0.07$) introduces

significant dissipation, reducing the dissipation peak, while $C_v = 0.01$ produces results nearly identical to the baseline case without SGS, only slightly mitigating the peak (Fig. 4a). In the spectral domain, $C_v = 0.07$ effectively suppresses energy accumulation at high wavenumbers ($k > 30$), but over-dissipates energy at intermediate scales and remains slightly insufficient near the Nyquist limit. Conversely, $C_v = 0.01$ does not provide adequate dissipation, and energy pile-up persists (Fig. 4b).

To examine this phenomenon in greater detail, Fig. 5 is presented. Each subplot in the figure contains two panels: the upper panel displays the energy spectra $E(k)$ for both configurations on a logarithmic scale, while the lower panel shows the spectral difference

$$\Delta E(k) = E_{\text{base}}(k) - E_{\text{SGS}}(k),$$

which quantifies the modification of the energy content across scales induced by the SGS model. Since the results are represented on logarithmic scales, the absolute value of the spectral difference is plotted in the lower panel. To retain information on the sign of $\Delta E(k)$, two reference lines are added. It should be noted that the simultaneous presence of positive and negative values indicates that the subgrid model has a negligible effect, with values oscillating around zero. Conversely, consistently positive values reveal that the SGS model drains energy from the resolved scales, allowing one to identify the wavenumber at which this energy removal becomes effective.

In both cases, the difference between simulations with and without the SGS model exhibits a similar trend. Up to a certain wavenumber, both spectra remain nearly identical, with the difference oscillating around zero. The magnitude of this difference scales with the model constant and remains much smaller than the flow energy at those wavenumbers, which explains its absence in the upper figures. For the weaker model, this transition occurs around $k \approx 30$, and for the stronger one, it occurs around $k \approx 20$. The model constant thus appears to control the range of resolved scales before the SGS model becomes active. Beyond this point, the turbulence model dissipates the energy accumulation near the cutoff wavenumber. The stronger model achieves this more effectively.

In summary, the inclusion of the Vreman SGS model does not enhance the transitional flow dynamics, and the solution quality in this regime remains limited. Once turbulence is developed, a larger model constant helps to achieve the expected spectral behavior. The intensity of dissipation at high wavenumbers depends on the specific wavenumber at which the model-induced dissipation becomes apparent. Consequently, intermediate scales tend to be over-damped when a large constant is used, while a smaller constant leaves the highest wavenumbers slightly under-dissipated.

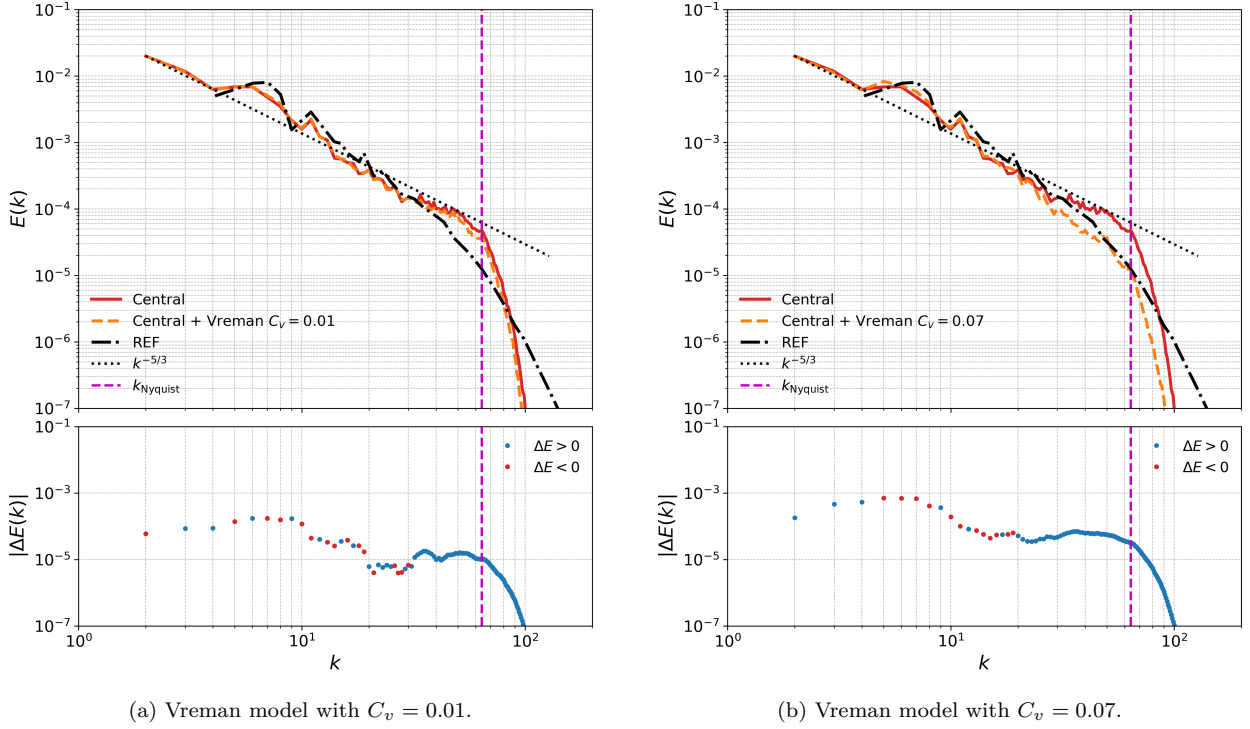


Figure 5: Comparison between the baseline central scheme and the same scheme augmented with a Vreman SGS model of different strengths for the TGV at Reynolds 1600. Each subfigure shows the energy spectra (top) and the spectral difference $\Delta E(k)$ (bottom). The figures highlight how the SGS model constant controls both the magnitude of the added dissipation and the wavenumber at which it becomes active.

4.1.4. Influence of Riemann Solvers

Riemann solvers introduce upwind dissipation through characteristic decomposition, producing an interesting iLES behavior. In this part, the Chandrasekhar split form is employed without explicit SGS modeling to isolate the effects of the Riemann solver choice.

During the transitional phase ($t/t_c \in [4, 8]$), Riemann solvers improve solution stability and accuracy. Central fluxes alone do not provide sufficient dissipation, and the split form compensates by introducing excessive implicit dissipation. The Roe and Matrix Dissipation fluxes yield smooth dissipation profiles that agree well with the reference solution. This observation is consistent with the findings of [76], who reported that Riemann solvers primarily influence the high-wavenumber dynamics.

The low-dissipation Roe (LD-Roe) solver provides an intermediate approach: it partially relies on the split form for early stabilization but ultimately introduces more dissipation than optimal (Fig. 6a). In the spectral domain (Fig. 6b), all schemes except the less dissipative ones (central and LD-Roe) accurately capture the energy spectrum up to $k \approx 30$, while these

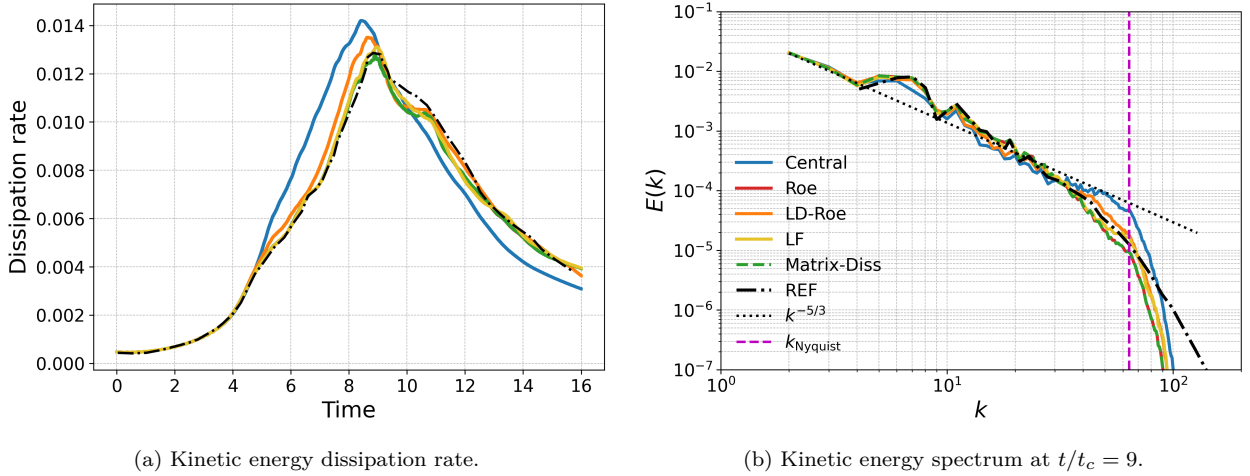


Figure 6: Effect of Riemann solver choice on dissipation and spectral behavior using the Chandrasekhar split form without explicit SGS modeling. Roe, Matrix Dissipation, and Lax–Friedrichs supply controlled high-wavenumber dissipation that stabilizes the transition and improves agreement with the reference solution, while central and LD-Roe fluxes remain under-dissipative in the turbulent regime.

flux formulations exhibit a slight loss of precision. For larger wavenumbers, the central flux exhibits strong energy pile-up; LD-Roe exhibits a minor energy pile-up, while Roe and Matrix Dissipation slightly over-dissipate the highest wavenumbers. The Lax–Friedrichs scheme performs similarly to Roe but differs in that it shows a noticeable energy accumulation near the cutoff due to its over-upwind character at low Mach numbers, as previously reported in [77, 21].

For the subsequent analysis, the Roe scheme (which exhibited the best overall performance) and its low-dissipation variant, LD-Roe, are retained to assess whether they can be fine-tuned by introducing a controlled amount of dissipation through the SGS model.

4.1.5. Hybrid iLES–SGS Configurations

Hybrid configurations combining Riemann solvers with a weak Vreman SGS model ($C_v = 0.01$) are evaluated to determine whether a small explicit viscosity improves transitional and turbulent dynamics.

With the low Vreman constant ($C_v = 0.01$), the explicit subgrid-scale contribution is minor. During the transitional phase ($t/t_c < 8$), a slight increase in dissipation is observed, most notably for the LD-Roe–Vreman configuration, which exhibits a marginally reduced dissipation peak. In contrast, the standard Roe flux shows negligible change, indicating that the iLES dissipation from the Riemann solver dominates.

Beyond $t/t_c = 8$, the simulations without Vreman maintain slightly elevated dissipation,

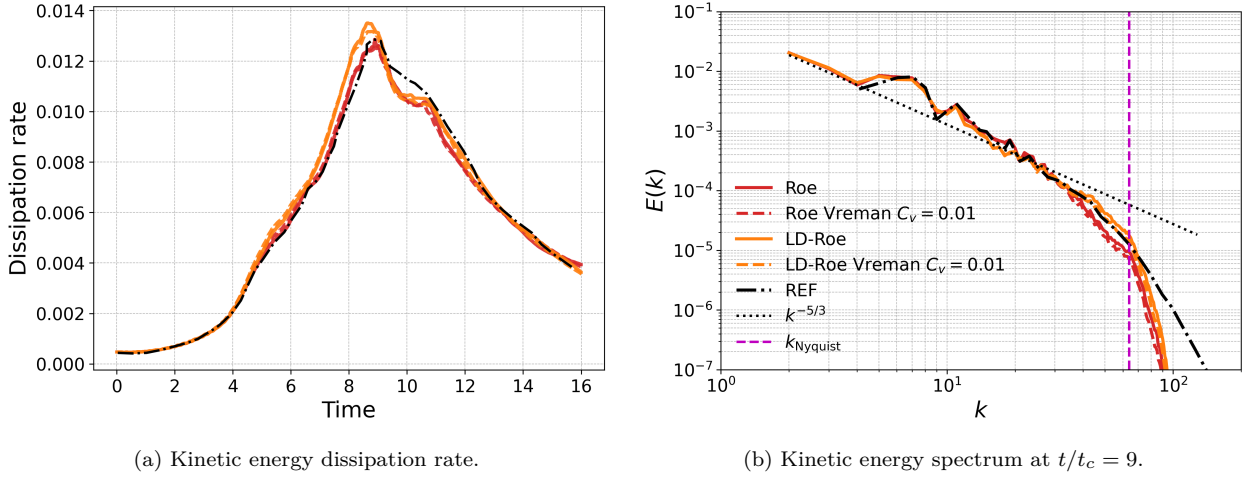


Figure 7: Effect of combining Riemann solvers with a weak Vreman SGS model ($C_v = 0.01$) on dissipation and spectral behavior. The weak SGS contribution slightly increases dissipation during transition, most noticeably for the LD-Roe–Vreman configuration, while the Roe flux remains largely unchanged. In the turbulent regime, LD-Roe coupled with the SGS model better mitigates energy pile-up at high wavenumbers, providing improved spectral fidelity compared to the purely iLES configurations.

subtly damping small-scale energy. Spectrally (Fig. 7b), all configurations behave similarly for well-resolved scales ($k < 30$). For higher wavenumbers ($k > 30$), LD-Roe–Vreman shows improved spectral agreement with reference, effectively mitigating energy pile-up at the smallest resolved scales.

In summary, the weak Vreman SGS model has a limited impact during the transitional phase, offering only marginal benefits when combined with LD-Roe. In this regime, the Roe flux remains the best performer. Once turbulence is fully developed, Roe tends to be slightly over-dissipative at high wavenumbers, while the LD-Roe scheme coupled with the Vreman model provides the best spectral fidelity.

4.2. Under-Resolved LES (The Inviscid Taylor–Green Vortex): Necessity and Limitations of Explicit SGS Models

In the previous section, it was shown that the weak Vreman SGS model has a minor influence during transition, with Roe providing the best overall performance. In the turbulent regime, Roe becomes slightly over-dissipative, while LD-Roe combined with Vreman achieves the highest spectral fidelity. To further assess the robustness and dissipation properties of these configurations, we now consider the inviscid Taylor–Green vortex (Euler limit). This case removes physical viscosity, thereby isolating the numerical dissipation mechanisms—implicit, through the Riemann solver and the Chandrasekhar split form, and explicit, through the

Vreman model—in stabilizing the flow and sustaining the energy cascade. The objective is to determine whether the same trends persist under inviscid conditions.

4.2.1. Hybrid iLES–SGS Configurations

We repeat the analysis from the previous section, combining the Riemann solvers with a weak Vreman SGS model ($C_v = 0.01$) and show the results in Fig. 8.

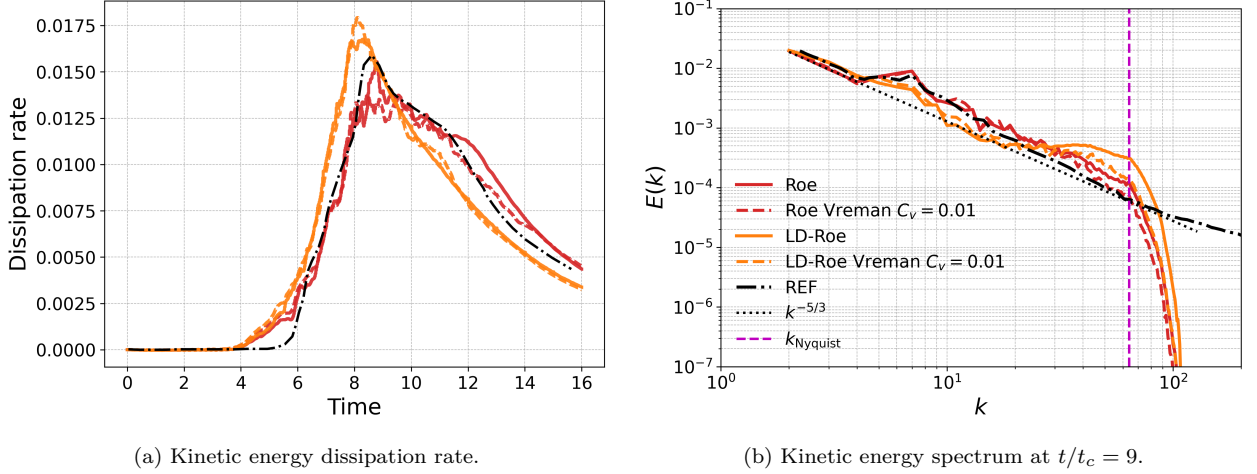


Figure 8: Inviscid TGV: Hybrid iLES–SGS configurations combining Riemann solvers with a weak Vreman model ($C_v = 0.01$). During transition, Roe without SGS best matches the high-resolution reference, while LD-Roe exhibits increased dissipation due to split-form activation. In the turbulent regime, the weak Vreman model improves high-wavenumber behavior for both fluxes. Overall, Roe provides the most consistent performance across both transitional and turbulent phases, with the weak SGS contribution mainly affecting small scales.

During the laminar phase ($t/t_c \lesssim 5$), all configurations exhibit similar behavior with minimal dissipation, and the weak Vreman SGS model has a negligible effect.

In the transitional regime ($t/t_c \gtrsim 5$), differences emerge. LD-Roe dissipates more energy due to the combination of insufficient built-in dissipation and the activation of the split form, while Roe remains closer to the high-resolution reference. The impact of Vreman differs between fluxes: for Roe, adding Vreman slightly decreases the dissipation peak, while for LD-Roe it slightly increases it. Overall, the best agreement with the high-resolution reference during transition is achieved by Roe without SGS.

In the fully developed turbulent phase, spectral behavior shows that Roe maintains energy levels reasonably well up to $k \approx 20$, while LD-Roe underestimates energy in this range and exhibits a high-wavenumber pile-up for $k > 20$. Adding Vreman to LD-Roe mitigates,

but does not completely remove, the pile-up. Roe–Vreman introduces extra dissipation for $k > 30$, improving high-wavenumber behavior.

In summary, Roe provides the most consistent performance across both transitional and turbulent stages in the inviscid TGV. The inclusion of a weak Vreman SGS model enhances dissipation at high wavenumbers, improving the turbulent regime but slightly reducing accuracy during transition. Notably, this conclusion differs from that of the viscous TGV case. In the following section, we refine the SGS constant to assess whether a higher value yields improved performance under inviscid conditions.

4.2.2. Fine-Tuning of the SGS Constant

In this section, we examine in detail the influence of the Vreman constant on the accuracy of the simulations. We retain the Roe flux, which exhibited the most consistent performance across the different regimes, and assess the impact of incorporating the Vreman model using two values of the constant: $C_v = 0.01$ and $C_v = 0.07$.

As observed previously, incorporating the Vreman model does not enhance performance during the transition phase. As shown in Fig. 9a, a small amount of Vreman dissipation ($C_v = 0.01$) already reduces accuracy, while increasing it to $C_v = 0.07$ further degrades the solution.

Focusing now on the energy spectra (Fig. 9b), the Roe scheme retains too much energy compared to the reference solution. Increasing the constant to $C_v = 0.01$ allows matching the reference near the cutoff, but leads to excessive energy between $k = 20$ and the cutoff wavenumber. In contrast, when increasing the constant to the typical finite-volume value of $C_v = 0.07$ aligns the spectrum around $k = 20$, but results in over-dissipation for $k > 20$.

To examine this phenomenon in greater detail, Fig. 10 quantifies the modification of the energy content across scales induced by the SGS model. Once again, the model with the lower constant adds dissipation at higher wavenumbers (compared to the model with the larger constant). The dissipation profiles appear flatter, likely due to the under-resolved (inviscid) nature of this test case. The profile is noticeably flatter for the higher-constant case. The higher constant leads to stronger overall dissipation—which is beneficial here—but ideally, one would want a distribution that increases dissipation around $k \approx 20$ (as in the $C_v = 0.07$ case) while reducing it near the cutoff wavenumber (as observed in the $C_v = 0.01$ case).

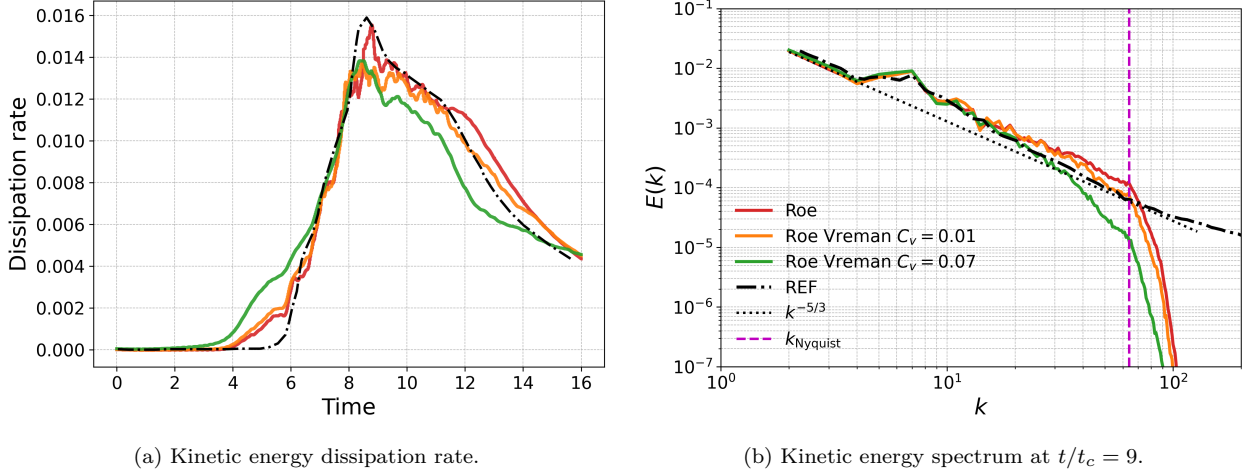


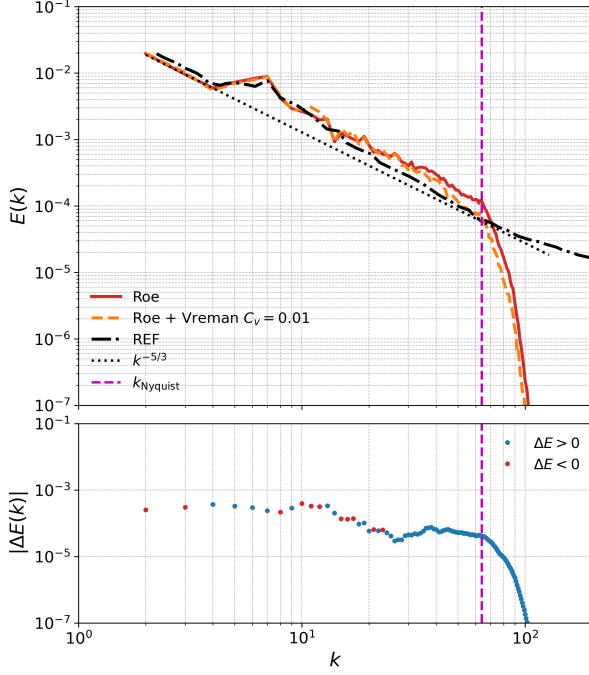
Figure 9: Inviscid TGV: Effect of the Vreman SGS constant on dissipation and spectral behavior for hybrid iLES–SGS configurations with the Roe flux. During transition, all SGS configurations reduce accuracy compared to the baseline Roe scheme. In the turbulent regime, a small constant ($C_v = 0.01$) mitigates high-wavenumber energy pile-up but overestimates energy at intermediate wavenumbers, while a larger constant ($C_v = 0.07$) improves dissipation around $k \approx 20$ but over-damps the highest wavenumbers.

5. Discussion: Challenges of Static Solver Configuration and traditional SGS in Transitional and Turbulent Flows

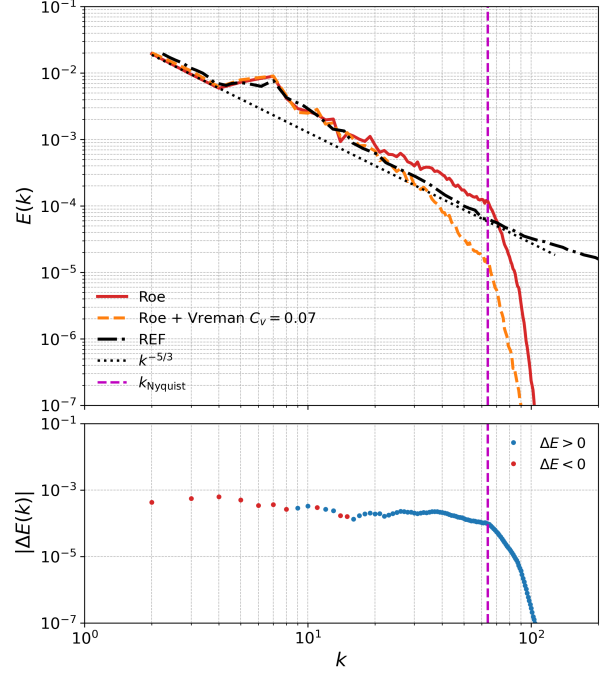
A recurring finding throughout this study is that there is no one unique combination of numerical parameters (split forms, fluxes, and SGS models) that performs optimally across all flow regimes: laminar, transitional, and turbulent. This limitation is particularly evident when comparing the behavior of Riemann solvers and SGS models during the transition and fully developed turbulence phases.

During transition, the Roe flux consistently yielded the best overall performance without requiring any SGS contribution. However, once turbulence developed, the dissipation provided by split forms and Riemann solvers alone was insufficient to maintain spectral balance. Weak SGS constants ($C_v = 0.01$) offered marginal improvements in the smallest resolved scales, while stronger constants ($C_v = 0.07$) introduced excessive dissipation, degrading intermediate wavenumbers. Moreover, the optimal SGS constant depends on the resolution level, as investigated here using both viscous and inviscid Taylor–Green Vortex cases.

These observations highlight the limitations of traditional SGS models in severely under-resolved, very high-order DG simulations. Although the accuracy of the solution improves by using SGS models, excessive SGS dissipation at intermediate scales can corrupt the solution near the cutoff wavenumber, especially in high-order discretizations where numerical



(a) Vreman model with $C_v = 0.01$.



(b) Vreman model with $C_v = 0.07$.

Figure 10: Comparison between the baseline Roe scheme and the same scheme augmented with a Vreman SGS model of different strengths for the inviscid TGV. Each subfigure shows the energy spectra (top) and the spectral difference $\Delta E(k)$ (bottom). The figures highlight how the SGS model constant controls both the magnitude of the added dissipation and the wavenumber at which it becomes active.

dissipation is minimal. This issue is less pronounced at lower orders, where the inherent numerical damping partially compensates for the deficiencies of the model.

The increasing reliance on GPU-based architectures is driving the adoption of very high polynomial orders, which expose fundamental limitations in current numerical and SGS models. Because high-order schemes exhibit low numerical dissipation up to the cutoff wavenumber, any poorly tuned SGS model can compromise an otherwise accurate simulation. Together, these findings emphasize the need for adaptive stabilization strategies both in space and in time. An example is spectral vanishing viscosity (SVV) [78], which has been previously combined with SGS modeling [76]. This approach allows dissipation to be targeted at specific wavenumbers, avoiding unnecessary damping elsewhere. Static configurations are insufficient to handle the evolving nature of transitional and turbulent flows. Future methodologies should incorporate scale-aware, case-specific mechanisms that dynamically balance dissipation between regimes (i.e., Reynolds numbers) and grid resolutions.

6. Conclusions

This work systematically examined the behavior of high-order discontinuous Galerkin discretizations for the three-dimensional Taylor–Green vortex ($Re = 1600$ and $Re \rightarrow \infty$), assessing the combined effects of split-form formulations, Riemann solvers, and explicit SGS models across both viscous and inviscid regimes. The study focuses on configurations driven by modern GPU-oriented architectures, which increasingly favor very high polynomial orders. This trend exposes intrinsic limitations in current numerical and subgrid-scale models that must be addressed to fully exploit the potential of high-order methods.

The results indicate that the optimal numerical configuration is highly sensitive to the flow regime and the resolution level. In well-resolved LES conditions, implicit dissipation mechanisms embedded in split forms and Riemann solvers are sufficient for accuracy and robustness. In contrast, under-resolved conditions require the use of SGS models to remove energy from high wavenumbers. Traditional SGS models can dissipate excessively at intermediate wavenumbers, degrading solutions that would otherwise be well resolved.

In summary, based on the analysis conducted, the optimal numerical configurations are identified as follows:

- **Well-resolved LES:** For the *transitional regime*, the most accurate configuration employs the split form (Chandrasekhar, though sensitivity to the specific form was negligible in our setup) combined with a Roe flux and no SGS model. In the *turbulent regime*, superior spectral fidelity is obtained using the split form and an LD-Roe flux, supplemented by an SGS model with a low constant ($C_v = 0.01$).
- **Under-resolved LES:** In the *transitional regime*, the best performance is again achieved using the split form (Chandrasekhar), Roe flux, and no SGS model. However, for the *turbulent regime*, the setup requires increased dissipation; the best spectral fidelity was observed using the split form and Roe flux with a higher SGS constant ($C_v = 0.07$). Note that as only $C_v = 0.01$ and $C_v = 0.07$ were tested, the global optimum for this specific problem may lie within this range.

Consequently, the development of adaptive stabilization mechanisms is a fundamental requirement to fully exploit the potential of high-order methods on next-generation computing architectures. Future work will focus on data-driven or AI-based methodologies to adaptively tune SGS constants or modify the SGS formulation itself, enabling scale-aware, case-specific stabilization that preserves spectral fidelity across a wider range of flow conditions. Moreover, since the scope of this study is limited to the Taylor–Green vortex, future investigations

will extend the analysis to wall-bounded simulations, such as channel flows, to assess the impact of wall effects on high-order DG methods and SGS modeling.

7. Acknowledgements

GR, GN, MCM, EV and EF acknowledge the funding received by the Grant DeepCFD (Project No. PID2022-137899OB-I00) funded by MICIU/AEI/10.13039/501100011033 and by ERDF, EU. This research has received funding from the European Union (ROSAS, project number 101138319). This research has received funding from the European Union (ERC, Off-coustics, project number 101086075). Views and opinions expressed are, however, those of the authors only and do not necessarily reflect those of the European Union or the European Research Council. Neither the European Union nor the granting authority can be held responsible for them. We thankfully acknowledge the computer resources at MareNostrum and the technical support provided by the Barcelona Supercomputing Center (RES-IM-2025-2-0013). All authors gratefully acknowledge the Universidad Polit cnica de Madrid (www.upm.es) for providing computing resources on the Magerit Supercomputer.

Appendix A. Navier–Stokes Equations

The 3D Navier-Stokes when including the Vreman model can be compactly written as:

$$\mathbf{u}_t + \nabla \cdot \vec{\mathbf{F}}_e = \nabla \cdot \vec{\mathbf{F}}_{v,turb}, \quad (\text{A.1})$$

where \mathbf{u} is the state vector of large scale resolved conservative variables $\mathbf{u} = [\rho, \rho v_1, \rho v_2, \rho v_3, \rho e]^T$, $\vec{\mathbf{F}}_e$ are the inviscid, or Euler fluxes,

$$\vec{\mathbf{F}}_e = \begin{bmatrix} \rho v_1 & \rho v_2 & \rho v_3 \\ \rho v_1^2 + p & \rho v_1 v_2 & \rho v_1 v_3 \\ \rho v_1 v_2 & \rho v_2^2 + p & \rho v_2 v_3 \\ \rho v_1 v_3 & \rho v_2 v_3 & \rho v_3^2 + p \\ \rho v_1 H & \rho v_2 H & \rho v_3 H \end{bmatrix}, \quad (\text{A.2})$$

where ρ , e , $H = E + p/\rho$, and p are the large scale density, total energy, total enthalpy and pressure, respectively, and $\vec{v} = [v_1, v_2, v_3]^T$ is the large scale resolved velocity components. Additionally, $\vec{\mathbf{F}}_{v,turb}$ defines the viscous and turbulent fluxes,

$$\vec{\mathbf{F}}_{v,turb} = \begin{bmatrix} 0 & 0 & 0 \\ \tau_{xx} & \tau_{xy} & \tau_{xz} \\ \tau_{yx} & \tau_{yy} & \tau_{yz} \\ \tau_{zx} & \tau_{zy} & \tau_{zz} \\ \sum_{j=1}^3 v_j \tau_{1j} + \kappa T_x & \sum_{j=1}^3 v_j \tau_{2j} + \kappa T_y & \sum_{j=1}^3 v_j \tau_{3j} + \kappa T_z \end{bmatrix}, \quad (\text{A.3})$$

where κ is the thermal conductivity, T_x, T_y and T_z denote the temperature gradients and the stress tensor $\boldsymbol{\tau}$ is defined as $\boldsymbol{\tau} = (\mu + \mu_t)(\nabla \vec{v} + (\nabla \vec{v})^T) - 2/3(\mu + \mu_t)\mathbf{I}\nabla \cdot \vec{v}$, with μ the dynamic viscosity, μ_t the turbulent viscosity (in this work defined through the Vreman model).

Appendix B. DGSEM

The physical domain is tessellated into non-overlapping curvilinear hexahedral elements, e , which are mapped to a reference element, el , using a polynomial transfinite mapping relating physical coordinates \vec{x} and reference coordinates $\vec{\xi}$. The transformed Navier–Stokes equations read:

$$J\mathbf{u}_t + \nabla_\xi \cdot \vec{\mathbf{F}}_e = \nabla_\xi \cdot \vec{\mathbf{F}}_v, \quad (\text{B.1})$$

where J is the Jacobian of the mapping, ∇_ξ denotes derivatives in the reference space, and $\vec{\mathbf{F}}$ are the contravariant fluxes [39].

Multiplying (B.1) by a smooth test function ϕ_j ($0 \leq j \leq P$, with P the polynomial degree) and integrating over an element yields the weak form:

$$\int_{el} J\mathbf{u}_t \phi_j + \int_{el} \nabla_\xi \cdot \vec{\mathbf{F}}_e \phi_j = \int_{el} \nabla_\xi \cdot \vec{\mathbf{F}}_v \phi_j. \quad (\text{B.2})$$

Integrating the inviscid flux term by parts separates surface and volume contributions:

$$\int_{el} J\mathbf{u}_t \phi_j + \int_{\partial el} \vec{\mathbf{F}}_e \cdot \hat{\mathbf{n}} \phi_j - \int_{el} \vec{\mathbf{F}}_e \cdot \nabla_\xi \phi_j = \int_{el} \nabla_\xi \cdot \vec{\mathbf{F}}_v \phi_j, \quad (\text{B.3})$$

where $\hat{\mathbf{n}}$ is the outward unit normal on element faces. Discontinuous inviscid fluxes at element interfaces are replaced by a numerical Riemann flux, $\vec{\mathbf{F}}_e^*$, to ensure inter-element coupling:

$$\int_{el} J\mathbf{u}_t \phi_j + \int_{\partial el} \vec{\mathbf{F}}_e^* \cdot \hat{\mathbf{n}} \phi_j - \int_{el} \vec{\mathbf{F}}_e \cdot \nabla_\xi \phi_j = \int_{el} \nabla_\xi \cdot \vec{\mathbf{F}}_v \phi_j. \quad (\text{B.4})$$

Viscous terms can be integrated by parts as well, leading to formulations such as BR1, BR2, or interior penalty; here, we retain the simple volume form for clarity. The final DGSEM discretization approximates solutions and fluxes with polynomials of degree P and evaluates volume and surface integrals using Gaussian quadrature. Gauss–Lobatto points enable energy/entropy-stable split forms, while Gauss–Legendre points provide higher quadrature accuracy.

Declaration of generative AI and AI-assisted technologies in the writing process

During the preparation of this work the author used OpenAI’s ChatGPT to correct grammar or spelling mistakes and to improve readability. After using this tool/service, the author(s) reviewed and edited the content as needed and take(s) full responsibility for the content of the publication.

References

- [1] J. S. Hesthaven, T. Warburton, Nodal Discontinuous Galerkin Methods, Springer New York, 2008. URL: <https://doi.org/10.1007/978-0-387-72067-8>. doi:10.1007/978-0-387-72067-8.
- [2] R. Moura, S. Sherwin, J. Peiro, Eigensolution analysis of spectral/hp continuous Galerkin approximations to advection-diffusion problems: Insights into spectral vanishing viscosity, *Journal of Computational Physics* 307 (2016) 401–422.
- [3] S. Sherwin, Dispersion analysis of the continuous and discontinuous Galerkin formulations., in: *International Symposium on Discontinuous Galerkin Methods*, Springer, 1999, pp. 425–431.
- [4] J. Manzanero, G. Rubio, E. Ferrer, E. Valero, Dispersion-dissipation analysis for advection problems with nonconstant coefficients: Applications to discontinuous Galerkin formulations, *SIAM Journal on Scientific Computing* 40 (2018) A747–A768.
- [5] C. Canuto, M. Y. Hussaini, A. Quarteroni, T. A. Zang, *Spectral Methods in Fluid Dynamics*, Springer Berlin Heidelberg, 1988. URL: <https://doi.org/10.1007/978-3-642-84108-8>. doi:10.1007/978-3-642-84108-8.
- [6] T. A. Zang, On the rotation and skew-symmetric forms for incompressible flow simulations, *Applied Numerical Mathematics* 7 (1991) 27–40.
- [7] G. Blaisdell, E. Spyropoulos, J. Qin, The effect of the formulation of nonlinear terms on aliasing errors in spectral methods, *Applied Numerical Mathematics* 21 (1996) 207–219.
- [8] E. Ferrer, An interior penalty stabilised incompressible discontinuous Galerkin Fourier solver for implicit large eddy simulations, *Journal of Computational Physics* 348 (2017) 754 – 775.

- [9] R. M. Kirby, S. J. Sherwin, Aliasing errors due to quadratic nonlinearities on triangular spectral /hp element discretisations, *Journal of Engineering Mathematics* 56 (2006) 273–288.
- [10] R. M. Kirby, G. E. Karniadakis, De-aliasing on non-uniform grids: algorithms and applications, *Journal of Computational Physics* 191 (2003) 249–264.
- [11] G. Mengaldo, D. D. Grazia, D. Moxey, P. Vincent, S. Sherwin, Dealiasing techniques for high-order spectral element methods on regular and irregular grids, *Journal of Computational Physics* 299 (2015) 56–81.
- [12] H. Blackburn, S. Schmidt, Spectral element filtering techniques for large eddy simulation with dynamic estimation, *Journal of Computational Physics* 186 (2003) 610 – 629.
- [13] T. C. Fisher, M. H. Carpenter, High-order entropy stable finite difference schemes for nonlinear conservation laws: Finite domains, *Journal of Computational Physics* 252 (2013) 518–557.
- [14] M. H. Carpenter, T. C. Fisher, E. J. Nielsen, S. H. Frankel, Entropy stable spectral collocation schemes for the Navier–Stokes equations: Discontinuous interfaces, *SIAM Journal on Scientific Computing* 36 (2014) B835–B867.
- [15] A. Schwarz, D. Kempf, J. Keim, P. Kopper, C. Rohde, A. Beck, Comparison of entropy stable collocation high-order DG methods for compressible turbulent flows, *Computers & Fluids* 303 (2025) 106874.
- [16] J. Manzanero, G. Rubio, D. A. Kopriva, E. Ferrer, E. Valero, An entropy–stable discontinuous Galerkin approximation for the incompressible Navier–Stokes equations with variable density and artificial compressibility, *Journal of Computational Physics* 408 (2020) 109241.
- [17] J. Manzanero, G. Rubio, D. A. Kopriva, E. Ferrer, E. Valero, A free–energy stable nodal discontinuous Galerkin approximation with summation–by–parts property for the Cahn–Hilliard equation, *Journal of Computational Physics* 403 (2020) 109072.
- [18] D. Lodaes, J. Manzanero, E. Ferrer, E. Valero, An entropy–stable discontinuous Galerkin approximation of the Spalart–Allmaras turbulence model for the compressible Reynolds Averaged Navier–Stokes equations, *Journal of Computational Physics* 455 (2022) 110998.

- [19] G. Ntoukas, J. Manzanero, G. Rubio, E. Valero, E. Ferrer, A free-energy stable p-adaptive nodal discontinuous Galerkin for the Cahn–Hilliard equation, *Journal of Computational Physics* 442 (2021) 110409.
- [20] G. Ntoukas, J. Manzanero, G. Rubio, E. Valero, E. Ferrer, An entropy-stable p-adaptive nodal discontinuous Galerkin for the coupled Navier–Stokes/Cahn–Hilliard system, *Journal of Computational Physics* 458 (2022) 111093.
- [21] A. R. Winters, R. C. Moura, G. Mengaldo, G. J. Gassner, S. Walch, J. Peiro, S. J. Sherwin, A comparative study on polynomial dealiasing and split form discontinuous Galerkin schemes for under-resolved turbulence computations, *Journal of Computational Physics* 372 (2018) 1–21.
- [22] J. Smagorinsky, General circulation experiments with the primitive equations: I. the basic experiment, *Monthly weather review* 91 (1963) 99–164.
- [23] D. K. Lilly, On the computational stability of numerical solutions of time-dependent non-linear geophysical fluid dynamics problems, *Monthly Weather Review* 93 (1965) 11–25.
- [24] F. Nicoud, F. Ducros, Subgrid-scale stress modelling based on the square of the velocity gradient tensor, *Flow, turbulence and Combustion* 62 (1999) 183–200.
- [25] A. Vreman, An eddy-viscosity subgrid-scale model for turbulent shear flow: Algebraic theory and applications, *Physics of fluids* 16 (2004) 3670–3681.
- [26] D. J. Garmann, M. R. Visbal, P. D. Orkwis, Comparative study of implicit and subgrid-scale model large-eddy simulation techniques for low-Reynolds number airfoil applications, *International Journal for Numerical Methods in Fluids* 71 (2013) 1546–1565.
- [27] Y. Li, Z. Wang, A priori and a posteriori evaluations of sub-grid scale models for the Burgers’ equation, *Computers & Fluids* 139 (2016) 92–104.
- [28] Z. Duan, Z. Wang, Calibrating sub-grid scale models for high-order wall-modeled large eddy simulation, *Advances in Aerodynamics* 6 (2024) 5.
- [29] T. Chatterjee, Y. T. Peet, Effect of artificial length scales in large eddy simulation of a neutral atmospheric boundary layer flow: A simple solution to log-layer mismatch, *Physics of Fluids* 29 (2017) 075105.

- [30] T. Mukha, P. Schlatter, Wall-modeled large-eddy simulation based on spectral-element discretization, arXiv preprint arXiv:2404.05378 (2024).
- [31] V. Kumar, O. Lehmkuhl, A. Tomboulides, P. Fischer, M. Min, Turbulence Modeling with Nek5000/RS, SOD2D and Alya, Technical Report, Argonne National Laboratory (ANL), Argonne, IL (United States), 2023.
- [32] S. Reddy, Y. Tissaoui, Comparison of sub-grid scale models for large-eddy simulation using a high-order spectral element approximation of the compressible Navier-Stokes equations at low Mach number, Technical Report, 2021.
- [33] G. Ntoukas, G. Rubio, O. A. Marino, A. Liosi, F. Bottone, J. Hoessler, E. Ferrer, A comparative study of explicit and implicit large eddy simulations using a high-order discontinuous Galerkin solver: Application to a Formula 1 front wing, Results in Engineering 25 (2025) 104425.
- [34] A. Beck, M. Kurz, Toward discretization-consistent closure schemes for large eddy simulation using reinforcement learning, Physics of Fluids 35 (2023) 125122.
- [35] M. Kurz, P. Offenhäuser, A. Beck, Deep reinforcement learning for turbulence modeling in large eddy simulations, International Journal of Heat and Fluid Flow 99 (2023) 109094.
- [36] N. Fehn, W. A. Wall, M. Kronbichler, Efficiency of high-performance discontinuous Galerkin spectral element methods for under-resolved turbulent incompressible flows, International Journal for Numerical Methods in Fluids 88 (2018) 32–54.
- [37] L. Gasparino, F. Spiga, O. Lehmkuhl, SOD2D: A GPU-enabled spectral finite elements method for compressible scale-resolving simulations, Computer Physics Communications 297 (2024) 109067.
- [38] HORSES3D: A high-order discontinuous Galerkin solver for flow simulations and multi-physics applications, <https://github.com/loganoz/horses3d-gpu>, 2025. Accessed: 2025-09-30.
- [39] D.A. Kopriva, Implementing spectral methods for partial differential equations, Springer Netherlands, 2009. URL: <http://dx.doi.org/10.1007/978-90-481-2261-5>. doi:10.1007/978-90-481-2261-5.

- [40] E. Ferrer, G. Rubio, G. Ntoukas, W. Laskowski, O. A. Mariño, S. Colombo, A. Mateo-Gabín, H. Marbona, F. M. de Lara, D. Huergo, et al., HORSES3D: A high-order discontinuous Galerkin solver for flow simulations and multi-physics applications, *Computer Physics Communications* 287 (2023) 108700.
- [41] G. Gassner, D. A. Kopriva, A comparison of the dispersion and dissipation errors of Gauss and Gauss–Lobatto discontinuous Galerkin spectral element methods, *SIAM Journal on Scientific Computing* 33 (2011) 2560–2579.
- [42] J. Manzanero, A. M. Rueda-Ramírez, G. Rubio, E. Ferrer, The Bassi Rebay 1 scheme is a special case of the symmetric interior penalty formulation for discontinuous Galerkin discretisations with Gauss–Lobatto points, *Journal of Computational Physics* 363 (2018) 1–10.
- [43] G. J. Gassner, A. R. Winters, F. J. Hindenlang, D. A. Kopriva, The BR1 scheme is stable for the compressible Navier–Stokes equations, *Journal of Scientific Computing* 77 (2018) 154–200.
- [44] D. Arnold, F. Brezzi, B. Cockburn, L. Marini, Unified analysis of discontinuous Galerkin methods for elliptic problems, *SIAM Journal of Numerical Analysis* 39 (2001) 1749–1779.
- [45] G. J. Gassner, A. D. Beck, On the accuracy of high-order discretizations for under-resolved turbulence simulations, *Theoretical and Computational Fluid Dynamics* 27 (2012) 221–237.
- [46] D.A. Kopriva and G.J. Gassner, An energy stable discontinuous Galerkin spectral element discretization for variable coefficient advection problems, *SIAM Journal on Scientific Computing* 36 (2014) A2076–A2099.
- [47] G. J. Gassner, A. R. Winters, D. A. Kopriva, Split form nodal discontinuous Galerkin schemes with summation-by-parts property for the compressible Euler equations, *Journal of Computational Physics* 327 (2016) 39–66.
- [48] J. Manzanero, G. Rubio, E. Ferrer, E. Valero, D. A. Kopriva, Insights on aliasing driven instabilities for advection equations with application to Gauss-Lobatto discontinuous Galerkin methods, *J. Sci. Comput.* 75 (2018) 1262–1281.
- [49] A. Mateo-Gabín, A. M. Rueda-Ramírez, E. Valero, G. Rubio, A flux-differencing formulation with Gauss nodes, *Journal of Computational Physics* 489 (2023) 112298.

- [50] D. A. Kopriva, G. J. Gassner, An energy stable discontinuous Galerkin spectral element discretization for variable coefficient advection problems, *SIAM Journal on Scientific Computing* 36 (2014) A2076–A2099.
- [51] G. J. Gassner, A. R. Winters, F. J. Hindenlang, D. A. Kopriva, The BR1 scheme is stable for the compressible Navier–Stokes equations, *Journal of Scientific Computing* 77 (2018) 154–200.
- [52] J. Manzanero, G. Rubio, D. A. Kopriva, E. Ferrer, E. Valero, Entropy–stable discontinuous Galerkin approximation with summation–by–parts property for the incompressible Navier–Stokes/Cahn–Hilliard system, *Journal of Computational Physics* (2020) 109363.
- [53] T. Chen, C.-W. Shu, Entropy stable high order discontinuous Galerkin methods with suitable quadrature rules for hyperbolic conservation laws, *Journal of Computational Physics* 345 (2017) 427–461.
- [54] G. J. Gassner, A skew-symmetric discontinuous Galerkin spectral element discretization and its relation to SBP-SAT finite difference methods, *SIAM Journal on Scientific Computing* 35 (2013) A1233–A1253.
- [55] A. R. Winters, D. A. Kopriva, G. J. Gassner, F. Hindenlang, Construction of modern robust nodal discontinuous Galerkin spectral element methods for the compressible Navier–Stokes equations, in: *Efficient High-Order Discretizations for Computational Fluid Dynamics*, Springer, 2021, pp. 117–196.
- [56] T. Chen, C.-W. Shu, Review of entropy stable discontinuous Galerkin methods for systems of conservation laws on unstructured simplex meshes, *CSIAM Trans. Appl. Math.* 1 (2020) 1–52.
- [57] Y. Morinishi, Skew-symmetric form of convective terms and fully conservative finite difference schemes for variable density low-mach number flows, *Journal of Computational Physics* 229 (2010) 276–300.
- [58] F. Ducros, F. Laporte, T. Soulères, V. Guinot, P. Moinat, B. Caruelle, High-order fluxes for conservative skew-symmetric-like schemes in structured meshes: Application to compressible flows, *Journal of Computational Physics* 161 (2000) 114–139.
- [59] C. A. Kennedy, A. Gruber, Reduced aliasing formulations of the convective terms within the Navier–Stokes equations for a compressible fluid, *Journal of Computational Physics* 227 (2008) 1676–1700.

- [60] S. Pirozzoli, Generalized conservative approximations of split convective derivative operators, *Journal of Computational Physics* 229 (2010) 7180–7190.
- [61] F. Ismail, P. L. Roe, Affordable, entropy-consistent euler flux functions II: Entropy production at shocks, *Journal of Computational Physics* 228 (2009) 5410–5436.
- [62] P. Chandrashekar, Kinetic energy preserving and entropy stable finite volume schemes for compressible Euler and Navier-Stokes equations, *Communications in Computational Physics* 14 (2013) 1252–1286.
- [63] Z. Wang, R. Fidkowski, K. Abgrall, F. Bassi, D. Caraeni, A. Cary, H. Deconinck, R. Hartmann, K. Hillewaert, H. Huynh, N. Kroll, G. May, P. Persson, B. van Leer, M. Visbal, High-order CFD methods: current status and perspective, *International Journal for Numerical Methods in Fluids* 72 (2013) 811–845.
- [64] A. Beck, T. Bolemann, D. Flad, H. Frank, G. Gassner, F. Hindenlang, C. Munz, High-order discontinuous Galerkin spectral element methods for transitional and turbulent flow simulations, *International Journal for Numerical Methods in Fluids* 76 (2014) 522–548.
- [65] D. Flad, G. Gassner, On the use of kinetic energy preserving DG-schemes for large eddy simulation, *Journal of Computational Physics* 350 (2017) 782 – 795.
- [66] J. Manzanero, E. Ferrer, G. Rubio, E. Valero, On the role of numerical dissipation in stabilising under-resolved turbulent simulations using discontinuous Galerkin methods, *arXiv:1805.10519* (2018).
- [67] E. F. Toro, *Riemann solvers and numerical methods for fluid dynamics: a practical introduction*, Springer Science & Business Media, 2013.
- [68] K. Oßwald, A. Siegmund, P. Birken, V. Hannemann, A. Meister, L2Roe: a low dissipation version of roe’s approximate riemann solver for low mach numbers, *International Journal for Numerical Methods in Fluids* 81 (2016) 71–86.
- [69] K. O. Friedrichs, P. D. Lax, Systems of conservation equations with a convex extension, *Proceedings of the National Academy of Sciences* 68 (1971) 1686–1688.
- [70] J. Williamson, Low-storage Runge-Kutta schemes, *Journal of Computational Physics* 35 (1980) 48–56.

- [71] N. Fehn, M. Kronbichler, P. Munch, W. A. Wall, Numerical evidence of anomalous energy dissipation in incompressible Euler flows: towards grid-converged results for the inviscid Taylor–Green problem, *Journal of Fluid Mechanics* 932 (2022) A40.
- [72] J. R. Bull, A. Jameson, Simulation of the Taylor–Green vortex using high-order flux reconstruction schemes, *AIAA Journal* 53 (2015) 2750–2761.
- [73] C. Carton De Wiart, K. Hillewaert, M. Duponcheel, G. Winckelmans, Assessment of a discontinuous Galerkin method for the simulation of vortical flows at high Reynolds number, *International Journal for Numerical Methods in Fluids* 74 (2014) 469–493.
- [74] A. Mateo-Gabin, K. Tlales, E. Valero, E. Ferrer, G. Rubio, An unsupervised machine-learning-based shock sensor: Application to high-order supersonic flow solvers, *Expert Systems with Applications* 270 (2025) 126352.
- [75] M. Vázquez, G. Houzeaux, S. Koric, A. Artigues, J. Aguado-Sierra, R. Arís, D. Mira, H. Calmet, F. Cucchietti, H. Owen, et al., Alya: Multiphysics engineering simulation toward exascale, *Journal of computational science* 14 (2016) 15–27.
- [76] J. Manzanero, E. Ferrer, G. Rubio, E. Valero, Design of a Smagorinsky spectral vanishing viscosity turbulence model for discontinuous Galerkin methods, *Computers & Fluids* 200 (2020) 104440.
- [77] R. C. Moura, G. Mengaldo, J. Peiró, S. J. Sherwin, An LES setting for DG-based implicit LES with insights on dissipation and robustness, in: *Spectral and High Order Methods for Partial Differential Equations ICOSAHOM 2016*, Springer, 2017, pp. 161–173.
- [78] R. M. Kirby, S. J. Sherwin, Stabilisation of spectral/hp element methods through spectral vanishing viscosity: Application to fluid mechanics modelling, *Computer methods in applied mechanics and engineering* 195 (2006) 3128–3144.